Available online at www.sciencedirect.com

ScienceDirect

Ceramics International 40 (2014) 3619–3625

CERAMICS INTERNATIONAL

www.elsevier.com/locate/ceramint

XRD cation distribution and magnetic properties of mesoporous Zn-substituted $CuFe_2O_4$

Najmeh Najmoddin[a,b], Ali Beitollahi[b], Hüseyin Kavas[c], Seyed Majid Mohseni[a], Hamidreza Rezaie[b], Johan Åkerman[a], Muhammet S. Toprak[a,*]

[a]Department of Materials and Nano Physics, KTH—Royal Institute of Technology, 16440 Kista-Stockholm, Sweden

[b]Center of Excellence for Ceramic Materials in Energy and Environment Applications, School of Metallurgy & Materials Engineering, Iran University of Science and Technology (IUST), Narmak, 16846 Tehran, Iran

[c]Department of Physics, Fatih University, Buyukcekmece, 34500 Istanbul, Turkey

Received 21 June 2013; received in revised form 11 September 2013; accepted 13 September 2013
Available online 19 September 2013

Abstract

The effect of Zn doping on magnetic properties of mesoporous $CuFe_2O_4$ has been investigated. The cation distribution amongst tetrahedral (A) and octahedral (B) sites of the lattice has been calculated analytically by X-ray diffraction (XRD), using the Bertaut method. The results reveal that these ferrites belong to the family of mixed or partially inverse spinels and Zn^{2+} ions occupy mainly the A site while Cu^{2+} ions have more tendency for the B-site. The magnetic moments estimated from cation distribution do not coincide with the magnetization data obtained from the SQUID-VSM technique. This is attributed to the core–shell structure of nanoparticles and non-collinearity of spins at the surface or spin canting in the sublattices of Zn-substituted $CuFe_2O_4$ nanoparticles. The temperature dependence of the zero field cooled (ZFC) and field cooled (FC) magnetization curves of mesoporous $Cu_{0.75}Zn_{0.25}Fe_2O_4$ confirms the presence of superparamagnetic phase at room temperature.

Keywords: C. Magnetic properties; D. Ferrites; Cation distribution; X-ray diffraction; Mesoporous materials

1. Introduction

Nanosized ferromagnetic cubic spinels, namely nanoferrites, have drawn considerable scientific and technological attention due to their distinct magnetic and electrical properties as compared to their bulk counterparts [1–3]. Nanocrystalline copper zinc ferrites have been extensively investigated due to their potential applications in non-resonant devices, radio frequency circuits, rod antennas, high quality filters and read/write heads for high-speed digital tapes [4–6]. The physical properties of ferrites depend significantly on the stoichiometry, preparation method as well as the distribution of cations among tetrahedral (A) and octahedral (B) sites [7–10]. Cation site occupancy is determined by factors such as ionic radius, crystal field, electronic configuration and ionic polarization [11].

During the past decades, many techniques have been exploited to study the cation distribution in spinel ferrites such as *R*-factor [12], Bertuat [13] and Furuhashi Monte Carlo methods [14]. All of them are based on the comparison between the XRD peak intensities observed experimentally and those calculated for a large number of hypothetical crystal structures.

The cation distribution of bulk CuZn and CuZnMn ferrites prepared by the solid state ceramic method has been reported by Rana et al. [12] and Birajdar et al. [15], respectively. Moussaoui et al. [4] studied the cation distribution of CuZn ferrite theoretically.

Herein, we report, for the first time, the cation distribution of mesoporous (MP) CuZn ferrite synthesized via confinement in the silica matrix, by the Bertuat method. We study the correlation between the data obtained from the XRD and magnetization evaluation. The magnetic characteristics have been evaluated in detail for the composition exhibiting the highest saturation magnetization.

*Corresponding author. Tel.: +46 73 5519358.
E-mail address: toprak@kth.se (M.S. Toprak).

0272-8842/$ - see front matter © 2013 Elsevier Ltd and Techna Group S.r.l. All rights reserved.
http://dx.doi.org/10.1016/j.ceramint.2013.09.063

2. Experimental

MP $Cu_{1-x}Zn_xFe_2O_4$ (where $x=0$, 0.25, 0.5, 0.75) were prepared by a novel nanocasting route. The procedure has been explained in detail elsewhere [16]. Briefly, vinyl-functionalized MP silica was impregnated by molten metal salts. After calcination at 600 °C for 6 h, the silica template was removed using 2 M NaOH aqueous solution. The MP nature of all samples were confirmed by low angle X-ray diffraction measurements (LXRD), N_2 adsorption–desorption and TEM analysis. Wide angle X-ray diffraction patterns (WXRD) of the powders were obtained using a XPERTPRO powder diffractometer (PANalytical, Almelo, The Netherlands) using CuKα radiation, $\lambda=1.5418$ Å, operating at 45 kV and 40 mA. Magnetic properties were characterized using a superconducting quantum interface device-vibrating sample magnetometer (SQUID-VSM) from Quantum Design, for temperature-dependent measurements ranging from 2 K to 300 K. The temperature dependence of the magnetization was determined in both field cooling (FC) and zero field cooling (ZFC) techniques. In the ZFC case, the sample was first cooled under zero magnetic field from 300 K down to 2 K and then a magnetic field was applied to the sample. The magnetic measurements were performed while the sample warmed up to 300 K. In the case of FC measurements, the sample was cooled down to 2 K in the presence of magnetic field and measurements were performed while the sample warmed up to 300 K.

3. Results and discussion

3.1. Structural properties

The WXRD patterns of all samples (Fig. 1) identified only the cubic spinel structure, showing that the samples formed in MP silica template have a high phase purity.

The lattice constant, a, measured as a function of Zn concentration exhibits an almost linear dependence, thus obeying Vegard's law. For an accurate calculation of the lattice constant, the lattice parameter was calculated for each peak of the XRD pattern and then the average of these values is reported.

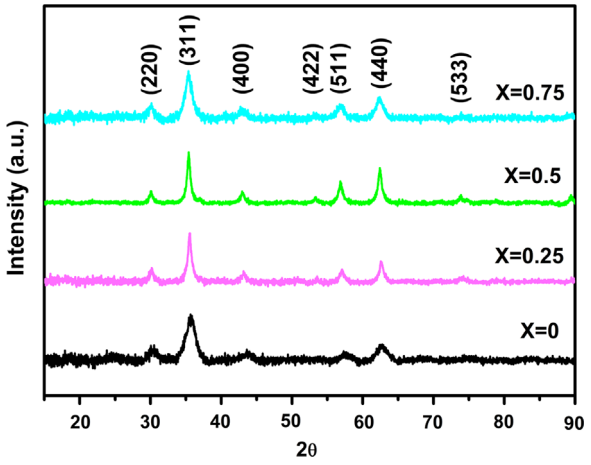

Fig. 1. Wide angle XRD patterns of MP $Cu_{1-x}Zn_xFe_2O_4$ (indexed to ICDD card no: 01-077-0010).

Table 1
Structural parameters of MP $Cu_{1-x}Zn_xFe_2O_4$.

Parameters	$x=0$	$x=0.25$	$x=0.5$	$x=0.75$
δ (nm)	6.57	8.21	8.27	6.95
a (Å)	8.34	8.39	8.40	8.42
ρ (g cm^{-3})	5.48	5.40	5.40	5.38

The peak broadening observed in the XRD patterns of all the samples reveals the small crystallite size, and was found to range from 6.5 to 8.3 nm, using the Scherrer equation. The lattice constant a, X-ray density d_x and crystallite size δ data are listed in Table 1.

3.2. Cation distribution

The cation distribution in MP $Cu_{1-x}Zn_xFe_2O_4$ can be estimated from the analysis of X-ray diffraction patterns. In the present study, the Bertaut method was used to determine the cation distribution. This method selects a few pairs of reflections according to the following expression:

$$\frac{I^{Obs.}_{hkl}}{I^{Obs.}_{h'k'l'}} = \frac{I^{Calc.}_{hkl}}{I^{Calc.}_{h'k'l'}} \quad (1)$$

where $I^{Obs.}$ and $I^{Calc.}$ are the observed and the calculated intensities for reflection (hkl), respectively [13]. Intensity ratios of some peak-pairs in the XRD pattern of spinel structures are known to be sensitive to cation distribution, such as I_{220}/I_{400}, I_{220}/I_{422} and I_{422}/I_{400}. An agreement factor, R, is defined by the following equation [13]:

$$R = \left| \left(\frac{I^{Obs.}_{hkl}}{I^{Obs.}_{h'k'l'}}\right) - \left(\frac{I^{Calc.}_{hkl}}{I^{Calc.}_{h'k'l'}}\right) \right| \quad (2)$$

The closest match with the actual sample structure, obtained by varying the cation distribution in the calculated intensity, will produce a minimum for R.

For the calculation of the relative integrated intensity of a given diffraction line from powder specimens as observed in a diffractometer with a flat plate sample holder, the following formula is used [9]:

$$I_{hkl} = |F_{hkl}|^2 \cdot P \cdot L_p \quad (3)$$

where F is the structure factor, P is the multiplicity factor and L_p is the Lorenz-polarization factor which depends only on Bragg's diffraction angle θ, described as follows [9]:

$$L_P = \frac{1+\cos^2 2\theta}{\sin^2\theta \cos 2\theta} \quad (4)$$

It should be noted that there is no need for the thermal correction because of the spinel's high melting point and hence very small thermo-vibration effect of spinel on XRD patterns.

The cation distribution for each Zn^{2+} content and the site preferences of cations distributed among A-site and B-site showing the fraction of Cu^{2+} and Fe^{3+} ions on either site are listed in Table 2. The distribution of cations among A and B sites in the substituted ferrite is proposed as $[Zn_{x-\alpha}Fe^{3+}_{1-x+\alpha-\beta}Cu^{2+}_{\beta}]^A$

Table 2
Cation distribution data from XRD and the saturation magnetization from SQUID for MP $Cu_{1-x}Zn_xFe_2O_4$.

Composition (x)	I_{220}/I_{400}		I_{422}/I_{400}		Cation distribution (XRD)	M_s (emu/g) (SQUID)
	Obs.	Calc.	Obs.	Calc.		
0.00	1.36	1.40	2.23	2.22	$(Cu_{0.00}\ Fe_{1.00})^A[Cu_{1.00}\ Fe_{1.00}]^B$	22
0.25	1.14	1.34	2.19	2.15	$(Zn_{0.00}\ Cu_{0.00}\ Fe_{1.00})^A\ [Zn_{0.25}\ Cu_{0.75}\ Fe_{1.00}]^B$	52
0.50	0.89	1.53	3.18	2.39	$(Zn_{0.30}\ Cu_{0.00}\ Fe_{0.70})^A\ [Zn_{0.20}\ Cu_{0.50}\ Fe_{1.30}]^B$	45
0.75	1.33	1.54	2.66	2.41	$(Zn_{0.17}\ Cu_{0.25}\ Fe_{0.58})^A\ [Zn_{0.58}\ Cu_{0.00}\ Fe_{1.42}]^B$	18

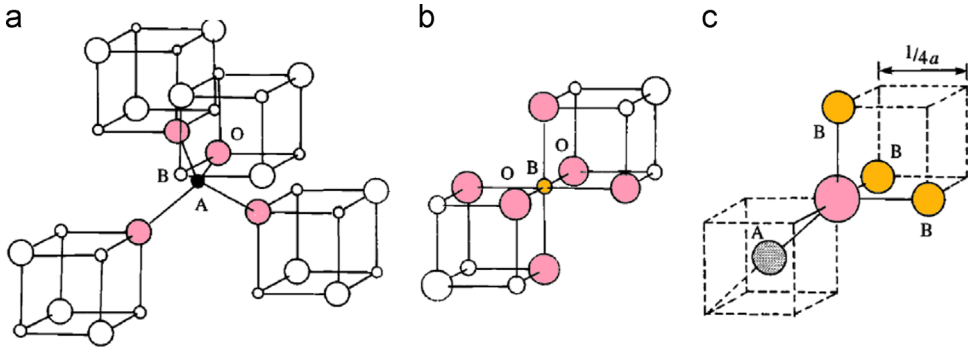

Fig. 2. Nearest neighbors of (a) a tetrahedral site, (b) an octahedral site and (c) an anion site (adapted from [11]).

$[Cu^{2+}_{1-x-\beta}Zn_\alpha Fe^{3+}_{1+x-\alpha+\beta}]^BO_4$ rather than $[Zn_xFe^{3+}_{1-x}]^A[Me^{2+}_{1-x}Fe^{3+}_{1+x}]^BO_4$ [17,18] as proposed by many others.

3.3. Ionic distances

To calculate the structure factors, a thorough understanding of the geometry of spinel structure is required. The unit cell in spinel structure contains 8 formula units of AB_2O_4, with 8 A sites, 16 B sites and 32 oxygen ions. Each A-site is surrounded by 4 O^{2-} and B-site by 6 O^{2-} ions (Fig. 2a and b). The O^{2-} ions have a four-fold coordination, formed by three B cations and one A cation (Fig. 2c).

Using the values of 'a', the radius of O^{2-} ion $r_O = 1.32$ Å [13] and the tetrahedral site radius 'r_A' in the following expression, the oxygen positional parameter, 'u', can be calculated as [13].

$$r_A = a\sqrt{3}(u-0.25) - r_O \quad (5)$$

The determined values of 'u' are listed in Table 3. The O^{2-} ions in the spinel structure are not generally located at the exact positions of the *fcc* sublattice. Their detailed positions are determined by u, which reflects adjustments of the structure to accommodate differences in the radius ratio of the cations in the A and B sites. The u parameter has a value of 0.375 and 0.25 for an ideal close-packed arrangement of O^{2-} ions for origins at $\bar{4}3m$ and $\bar{3}m$ (center of symmetry), respectively [11]. The ideal situation is almost never realized, and the u value for the vast majority of the known spinels is greater than 0.375 as can be seen in Table 3. u increases because the anions in A sites are forced to move in the [111] direction to give space to the A cations, which are almost always larger than the ideal space allowed by the close-packed oxygen.

Table 3
X-ray parameters: tetrahedral and octahedral bond lengths (d_{AL} and d_{BL}) and hopping lengths (L_A and L_B), tetrahedral edge d_{AE}, shared and unshared octahedral edges (d_{BE} and d_{BEU}) and oxygen positional parameter (u).

x	d_{AL} (Å)	d_{BL} (Å)	d_{AE} (Å)	d_{BE} (Å)	d_{BEU} (Å)	L_A (Å)	L_B (Å)	r_A (Å)	u (Å)
0.00	1.9935	1.9825	3.2553	2.6420	2.9566	3.6113	2.9486	0.670	0.397
0.25	1.9909	2.0019	3.2511	2.6815	2.9731	3.6330	2.9663	0.670	0.396
0.50	2.0369	1.9820	3.3262	2.6135	2.9805	3.6373	2.9698	0.718	0.398
0.75	2.0272	1.9941	3.3103	2.6435	2.9862	3.6460	2.9769	0.710	0.398

The values of the tetrahedral (d_{AL}), octahedral bond length (d_{BL}), tetrahedral edge length (d_{AE}), and shared (d_{BE}) and unshared octahedral edge lengths (d_{BEU}) were calculated by using the experimental values of lattice constant 'a' and oxygen positional parameter 'u' from the following equations [7]:

$$d_{AL} = a\sqrt{3}(u-0.25) \quad (6)$$

$$d_{BL} = a\sqrt{\left(3u^2 - \tfrac{11}{4}u + \tfrac{43}{64}\right)} \quad (7)$$

$$d_{AE} = a\sqrt{2}(2u-0.5) \quad (8)$$

$$d_{BE} = a\sqrt{2}(1-2u) \quad (9)$$

$$d_{BEU} = a\sqrt{\left(4u^2 - 3u + \tfrac{11}{16}\right)} \quad (10)$$

The data are presented in Table 3. The variation of the allied parameter could be related to the larger radius of Zn^{2+} ions as compared to Cu^{2+} ions and the site occupancy of the constituent ions in the present ferrite system.

It has been reported that the distance between the magnetic ions, known as hopping length L, influences the physical properties of the ferrite system. The hopping length for A-site (L_A) and B-site (L_B) is calculated using the values of lattice constant according to Eqs. (11) and (12), respectively [7]:

$$L_A = a\frac{\sqrt{3}}{4} \quad (11)$$

$$L_B = a\frac{\sqrt{2}}{4} \quad (12)$$

According to Table 3, L_A and L_B increase as Zn content x increases. This increase of hopping length with x is analogous to the increase of a with respect to x. This increase may be attributed to the difference in the ionic radii of the constituent ions, which increases the distances between the magnetic ions.

3.4. Magnetic properties

The magnetization of CuZn ferrites as a function of external field between ± 15 kOe at 300 K was studied. The observed hysteresis loops from VSM-SQUID are shown in Fig. 3. As can be seen, the maximum saturation magnetization is reached for the sample with $x=0.25$.

Table 4 shows the values of saturation magnetization, M_s, at room temperature. Using these values, the magnetic moment per formula unit in Bohr magneton (μ_B) was calculated with the following equation [9]:

$$n_B = \frac{M_{wt} \times M_s}{5585} \quad (13)$$

These results are also summarized in Table 4 as the observed magneton number with SQUID. The net magnetic moments of the spinel can also be calculated on the basis of cation distribution among A- and B-sites of the lattice. In ferrites, the magnetic ions on the A and B sites can be considered to be ferromagnetically coupled within each sublattice, and antiferromagnetically coupled between the sublattices [19]. The ionic magnetic moments of Fe^{3+}, Cu^{2+} and Zn^{2+} are 5 μ_B, 1 μ_B and 0 μ_B, respectively. The net magnetic moment values collected on the basis of cation distribution (A–B interaction) are listed in Table 4.

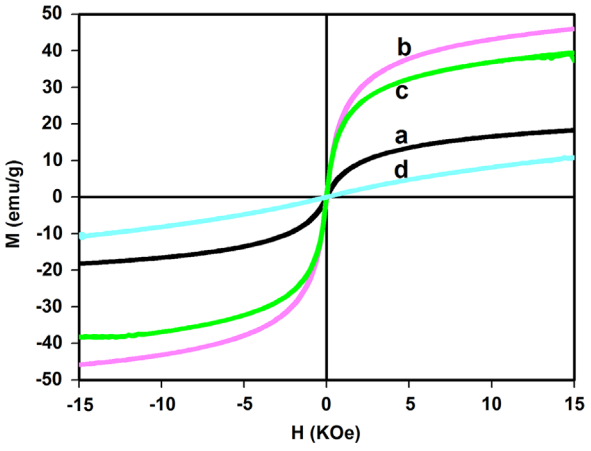

Fig. 3. Hysteresis loops of MP $Cu_{1-x}Zn_xFe_2O_4$ for x of (a) 0, (b) 0.25, (c) 0.5, and (d) 0.75, measured at 300 K.

Table 4
The magnetic moment per unit formula from XRD and SQUID data for MP $Cu_{1-x}Zn_xFe_2O_4$.

Magnetic number (μ_B)	$x=0$	$x=0.25$	$x=0.5$	$x=0.75$
Obs. (SQUID)	0.96	2.21	1.94	0.76
Calc. (XRD)	1	0.75	3.5	3.95

Table 5
Crystallite size (δ) obtained from XRD and magnetic core diameter (D_M) measured from magnetization hysteresis curves using Langevin equation for MP $Cu_{1-x}Zn_xFe_2O_4$.

Samples	$x=0$	$x=0.25$	$x=0.5$	$x=0.75$
δ (nm) (XRD)	6.57	8.21	8.27	6.95
D_M (nm) (SQUID)	6.46	8.07	8.04	5.61

The data obtained from XRD cation distribution do not coincide with the magnetization data obtained from the VSM-SQUID measurement especially at higher Zn concentration. This may be caused by the follwing:

(i) Finite size scaling which leads to a non-collinearity of magnetic moments on their surface due to broken exchange bonds at the external layer of the so-called core–shell nanoparticles, which consist of magnetically ordered core and disordered surface layers (the surface spin having nearest neighbors on one side and none on the other side) [20,21].

Magnetization curves were fitted according to the size distributed Langevin function [22] to determine the magnetic domain size. The mean magnetic domain size is given in Table 5 along with the crystallite size obtained from XRD. As can be seen, the mesoporous samples have a crystalline form with the mean dimensions in the range of 6.57–8.27 nm and a magnetic core with smaller dimensions. This implies that the magnetic core of particles is surrounded by a disordered surface layer, forming magnetic core–shell nanoparticles.

(ii) Non-equilibrium distribution of the cations amongst the interstitial spinel sites which lead to a non-collinear arrangement of the magnetic moments in A and B sites resulting from competing antiferromagnetic interactions and leading to the well-known canted Yafet–Kittel ferromagnetic structure [19,23].

Since the sample with Zn concentration of 0.25 showed higher saturation magnetization in this series, we studied its magnetic properties in detail. The magnetization of MP $Cu_{0.75}Zn_{0.25}Fe_2O_4$ at different temperatures is shown in Fig. 4. At 300 K, the coercive fields and remanences of the sample are almost negligible indicating superparamagnetic behavior.

By decreasing the temperature from 300 K to 2 K, the M_s value increases due to a decrease in the effects of thermal fluctuations on magnetic ions.

The high-field irreversibility and non-saturation behavior of magnetization observed in hysteresis loops at lower temperatures

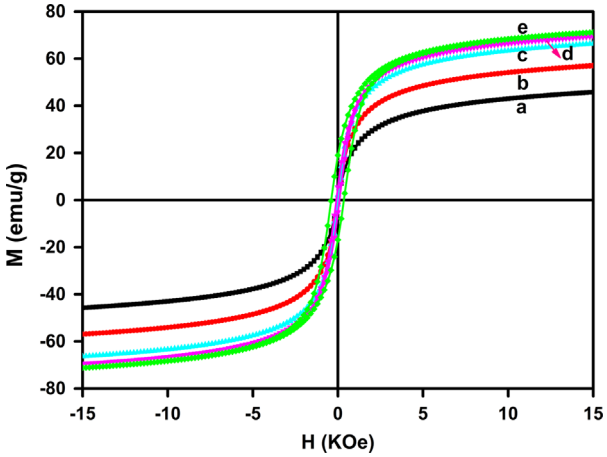

Fig. 4. Hysteresis loops of MP $Cu_{0.75}Zn_{0.25}Fe_2O_4$ measured at (a) 300 K, (b) 200 K, (c) 100 K, (d) 50 K and (e) 2 K.

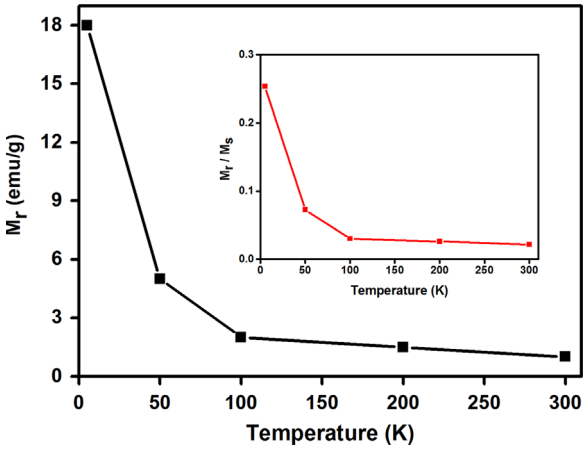

Fig. 5. The remanence magnetization, M_r, versus temperature for MP $Cu_{0.75}Zn_{0.25}Fe_2O_4$. Inset presents the change in reduced magnetization (M_r/M_s) with temperature.

indicate the existence of ordered core spins and canted or disordered surface spins due to broken symmetry for antiferromagnetic interactions. Due to strong coupling or pinning between disordered surface spins and ordered core spins, these disordered surface spins are not easily aligned even by high applied field [20].

The variation of remanence magnetization, M_r, with temperature for MP $Cu_{0.75}Zn_{0.25}Fe_2O_4$ is shown in Fig. 5. The inset in Fig. 5 shows the change in the reduced remanent magnetization (M_r/M_s) with the temperature.

The M_r/M_s values are less than 0.5, which are more in agreement with uniaxial anisotropy rather than the expected cubic anisotropy according to the Stoner–Wohlfarth model [19]. Therefore, the following equation is used for the calculation of the effective anisotropy constants K_{eff} [24]:

$$H_c = 0.985 \frac{K_{eff}}{M_s} \quad (14)$$

Temperature dependence of K_{eff} and coercivity H_c for the MP $Cu_{0.75}Zn_{0.25}Fe_2O_4$ is plotted in Fig. 6. Both K_{eff} and H_c increased with the decreasing temperature. The coercivity is

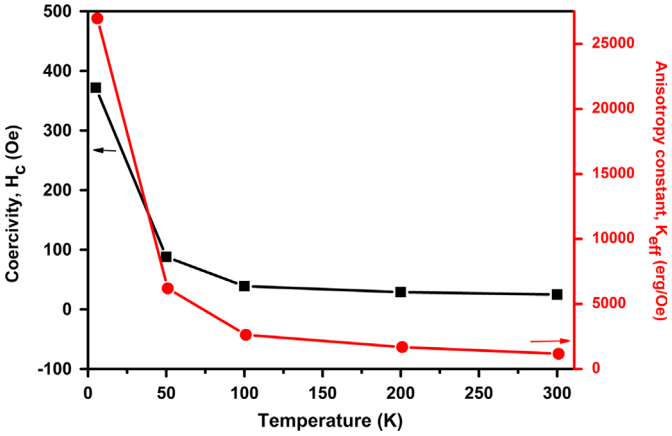

Fig. 6. Variation in anisotropy constant k_{eff} and coercivity H_c with temperature for MP $Cu_{0.75}Zn_{0.25}Fe_2O_4$.

associated to the strength of the magnetic field that is required to overcome the anisotropy barrier. According to the Stoner–Wohlfarth theory, magnetic anisotropy energy E_A, for non-interacting single-domain particles, is given by the following equation:

$$E_A = KV \sin^2 \theta \quad (15)$$

where K is the magnetocrystalline anisotropy constant and can be treated as the anisotropy energy per unit volume, V is the volume of the nanoparticle, and θ is the angle between the magnetization direction and the easy axis of the nanoparticles [25]. With reducing magnetic anisotropy E_A decreases, which causes lower external magnetic field for spin reversal resulting in reduction of H_c.

Fig. 7 shows ZFC/FC magnetization curves obtained at different applied fields for the MP $Cu_{0.75}Zn_{0.25}Fe_2O_4$. As the temperature increases in ZFC measurement, initially, the M_{ZFC} increases and reaches a maximum value at certain temperature which is called blocking temperature T_B. Above T_B, in the unblocked region, the M_{ZFC} monotonically decreases with the increasing temperature. This result further verified the superparamagnetic characteristics of MP $Cu_{0.75}Zn_{0.25}Fe_2O_4$ at room temperature. In the FC curves, M_{FC} decreases monotonously with the increasing temperature [26–28].

All ZFC/FC curves show an irreversible magnetic behavior below the temperature, called irreversibility temperature 'T_{irr}', for all the applied fields. T_{irr} is the temperature at which the ZFC and FC curves begin to separate, corresponding to the blocking or unblocking temperature of the largest particles. The difference $T_{irr} - T_B$ is therefore a qualitative indication of the width of the energy barrier distribution and thus of the nanoparticle size distribution [29]. T_{irr} and T_B shift to lower temperatures as the applied field increases. The ZFC magnetization curves around T_B lose their sharpness and become broader with the increasing field. The ZFC peak finally disappears at the applied field of 5 kOe but the irreversibility between the two curves continues even at that field. The observed high-field irreversibility in ZFC and FC magnetization curves is related to spin-glass-like behavior of the MP

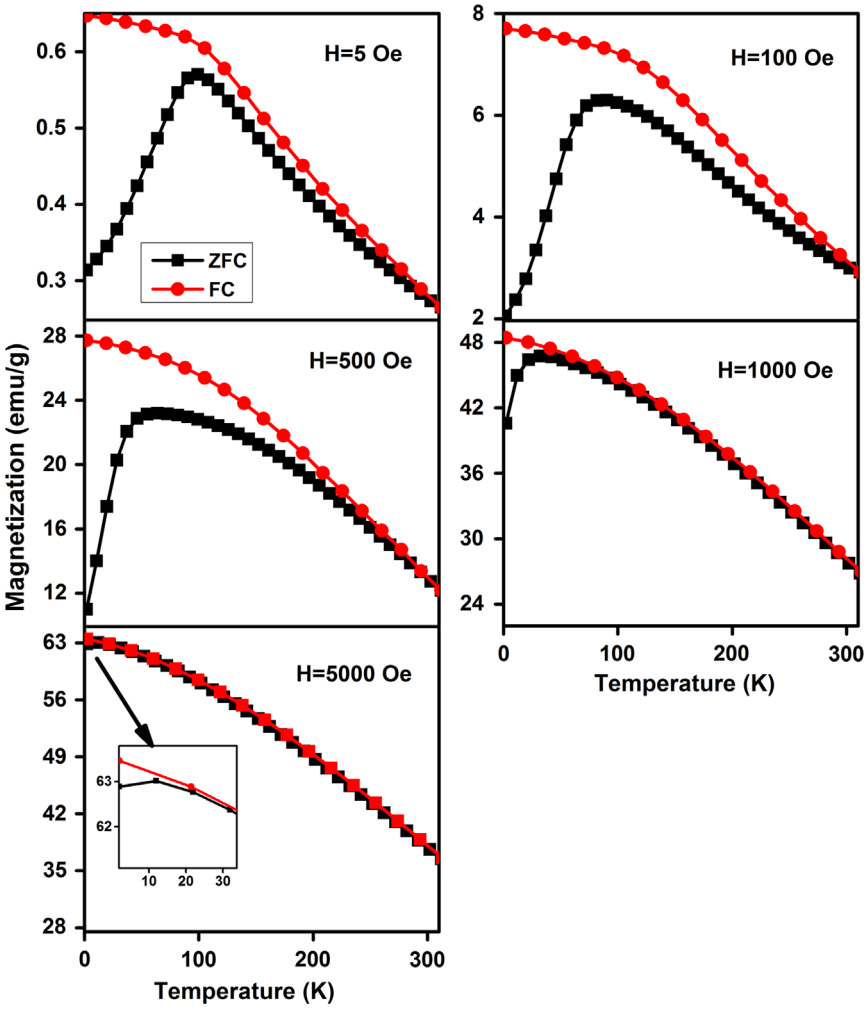

Fig. 7. Temperature- and field-dependent ZFC and FC magnetization curves of the MP $Cu_{0.75}Zn_{0.25}Fe_2O_4$.

$Cu_{0.75}Zn_{0.25}Fe_2O_4$ which is caused by disordered surface spins in core–shell ferrite nanoparticles.

4. Conclusion

The distribution of cations in the MP Zn-substituted copper ferrites was studied using the Bertaut method. This study revealed that these ferrites belong to a family of mixed or partially inverted spinels. Zn^{2+} ions showed a higher tendency to occupy A sites while Cu^{2+} ions accommodated mainly in B-sites. The difference between the magnetic moment of samples calculated from XRD cation distribution and measured from SQUID-VSM was attributed to the surface spin disorder or the spin canting in the sublattices. The magnetization evaluation for MP $Cu_{0.75}Zn_{0.25}Fe_2O_4$ indicated the presence of superparamagnetic phase at room temperature. The high-field irreversibility in ZFC/FC curves was the evidence of spin-glass-like surface layer in the MP $Cu_{0.75}Zn_{0.25}Fe_2O_4$.

References

[1] V. Blanco-Gutiérrez, J.A. Gallastegui, P. Bonville, M.J. Torralvo-Fernández, R. Sáez-Puche, MFe_2O_4: (MCo^{2+}, Ni^{2+}) nanoparticles: Mössbauer and X-ray absorption spectroscopies studies and high-temperature superparamagnetic behavior, Journal of Physical Chemistry C, 116, 24331–24339.

[2] S. Kumar, V. Singh, S. Aggarwal, U.K. Mandal, R.K. Kotnala, Influence of processing methodology on magnetic behavior of multicomponent ferrite nanocrystals, Journal of Physical Chemistry C 114 (2010) 6272–6280.

[3] C. Reitz, C. Suchomski, J. Haetge, T. Leichtweiss, Z. Jagličić, I. Djerdj, T. Brezesinski, Soft-templating synthesis of mesoporous magnetic $CuFe_2O_4$ thin films with ordered 3D honeycomb structure and partially inverted nanocrystalline spinel domains, Chemical Communications 48 (2012) 4471–4473.

[4] H.EI. Moussaoui, R. Masrour, O. Mounkachi, M. Hamedoun, A. Benyoussef, Cation distribution and magnetic interactions in Zn-substituted $Fe(Cu)Fe_2O_4$ ferrites, Journal of Superconductivity and Novel Magnetism 25 (2012) 2473–2480.

[5] P.P. Hankare, M.R. Kadam, R.P. Patil, K.M. Garadkar, R. Sasikala, A.K. Tripathi, Effect of zinc substitution on structural and magnetic properties of copper ferrite, Journal of Alloys and Compounds 501 (2010) 37–41.

[6] M. Ajmal, A. Maqsood, Structural, electrical and magnetic properties of $Cu_{1-x}Zn_xFe_2O_4$ ferrites ($0 \le x \le 1$), Journal of Alloys and Compounds 460 (2008) 54–59.

[7] I. Ahmad, T. Abbas, M.U. Islam, A. Maqsood, Study of cation distribution for Cu–Co nanoferrites synthesized by the sol–gel method, Ceramics International 39 (2013) 6735–6741.

[8] A. Hussain, T. Abbas, S.B. Niazi, Preparation of $Ni_{1-x}Mn_xFe_2O_4$ ferrites by sol–gel method and study of their cation distribution, Ceramics International 39 (2013) 1221–1225.
[9] H. Kavas, A. Baykal, M.S. Toprak, Y. Köseoğlu, M. Sertkol, B. Aktaş, Cation distribution and magnetic properties of Zn doped $NiFe_2O_4$ nanoparticles synthesized by PEG-assisted hydrothermal route, Journal of Alloys and Compounds 479 (2009) 49–55.
[10] R. Rani, S.K. Sharma, K.R. Pirota, M. Knobel, S. Thakur, M. Singh, Effect of zinc concentration on the magnetic properties of cobalt–zinc nanoferrite, Ceramics International 38 (2012) 2389–2394.
[11] R. Valenzuela, Magnetic Ceramics, Cambridge University Press, Cambridge, UK, 1994.
[12] M.U. Rana, M. Islam, T. Abbas, Cation distribution and magnetic interactions in Zn-substituted $CuFe_2O_4$ ferrites, Materials Chemistry and Physics 65 (2000) 345–349.
[13] D.R. Mane, D.D. Birajdar, S. Patil, S.E. Shirsath, R.H. Kadam, Redistribution of cations and enhancement in magnetic properties of sol–gel synthesized $Cu_{0.7-x}Co_xZn_{0.3}Fe_2O_4$ $(0 \le x \le 0.5)$, Journal of Sol–Gel Science and Technology 58 (2011) 70–79.
[14] H. Furuhashi, M. Inagaki, S. Naka, Determination of cation distribution in spinels by X-ray diffraction method, Journal of Inorganic and Nuclear Chemistry 35 (1973) 3009–3014.
[15] D.S. Birajdar, D.R. Mane, S.S. More, V.B. Kawade, K.M. Jadhav, Structural and magnetic properties of $Zn_xCu_{1.4-x}Mn_{0.4}Fe_{1.2}O_4$ ferrites, Materials Letters 59 (2005) 2981–2985.
[16] N. Najmoddin, A. Beitollahi, E. Devlin, H. Kavas, S.M. Mohseni, J. Åkerman, D. Niarchos, H. Rezaie, M. Muhammed, M.S. Toprak, Synthesis and magnetic properties of crystalline mesoporous Zn-substituted copper ferrite under nanoconfinement in silica matrix. Microporous and Mesoporous Materials, submitted for publication.
[17] T.J. Shinde, A.B. Gadkari, P.N. Vasambekar, Magnetic properties and cation distribution study of nanocrystalline Ni–Zn ferrites, Journal of Magnetism and Magnetic Materials 333 (2013) 152–155.
[18] T. Anjaneyulu, M.P. Narayana, K.K. Vijaya, Structural and magnetic properties of $Cu_{1-x}Zn_xFe_2O_4$ nano-powders synthesized by oxalate based precursor method, International Journal of Basic and Applied Chemical Sciences 3 (1) (2013) 50–59.
[19] R. Topkaya, A. Baykal, A. Demir, Yafet–Kittel-type magnetic order in Zn-substituted cobalt ferrite nanoparticles with uniaxial anisotropy, Journal of Nanoparticle Research 15 (2013) 1359.
[20] R. Topkaya, Ö. Akman, S. Kazan, B. Aktaş, Z. Durmus, A. Baykal, Surface spin disorder and spin-glass-like behaviour in manganese-substituted cobalt ferrite nanoparticles, Journal of Nanoparticle Research 14 (2012) 1156.
[21] J.M.D. Coey, Noncollinear spin arrangement in ultrafine ferrimagnetic crystallites, Physical Review Letters 27 (1971) 1140–1142.
[22] S. Laurent, D. Forge, M. Port, A. Roch, C. Robic, L.V. Elst, R.N. Muller, Magnetic iron oxide nanoparticles: synthesis, stabilization, vectorization, physicochemical characterizations, and biological applications, Chemical Reviews 108 (6) (2008) 2064 (–110).
[23] S. Ammar, N. Jouini, F. Fiévet, Z. Beji, L. Smiri, P. Moliné, M. Danot, J. Grenèche, Magnetic properties of zinc ferrite nanoparticles synthesized by hydrolysis in a polyol medium, Journal of Physics: Condensed Matter 18 (2006) 9055–9069.
[24] S.S. Jadhav, S.E. Shirsath, S.M. Patange, K.M. Jadhav, Effect of Zn substitution on magnetic properties of nanocrystalline cobalt ferrite, Journal of Applied Physics 108 (2010) 093920.
[25] A.J. Rondinone, A.C.S. Samia, Z.J. Zhang, Characterizing the magnetic anisotropy constant of spinel cobalt ferrite nanoparticles, Applied Physics Letters 76 (24) (2000) 3624–3626.
[26] M. Sertkol, Y. Köseoğlu, A. Baykal, H. Kavas, M.S. Toprak, Synthesis and magnetic characterization of $Zn_{0.7}Ni_{0.3}Fe_2O_4$ nanoparticles via microwave-assisted combustion route, Journal of Magnetism and Magnetic Materials 322 (2010) 866–871.
[27] Y. Köseoğlu, M. Bay, M. Tan, A. Baykal, H. Sözari, R. Topkaya, N. Akdoğan, Magnetic and dielectric properties of $Mn_{0.2}Ni_{0.8}Fe_2O_4$ nanoparticles synthesized by PEG-assisted hydrothermal method, Journal of Nanoparticle Research 13 (2011) 2235–2244.
[28] E.M.M. Ibrahim, S. Hample, A.U.B. Wollter, M. Kath, A.A. El-Gendy, R. Klingeler, C. Täschner, V.O. Khavrus, T. Gemming, A. Leonhardt, B. Büchner, Superparamagnetic FeCo and FeNi nanocomposites dispersed in submicrometer-sized C spheres, Journal of Physical Chemistry C 116 (2012) 22509–22517.
[29] C. Cannas, M.F. Casula, G. Concas, A. Corrias, D. Gatteschi, A. Falqui, A. Musinu, C. Sangregorio, G. Spano, Magnetic properties of γ-Fe_2O_3–SiO_2 aerogel and xerogel nanocomposite materials, Journal of Materials Chemistry 11 (2001) 3180–3187.